

State-to-state rotational rate constants for CO+He: Infrared double resonance measurements and simulation of the data using the SAPT theoretical potential energy surface

Tony C. Smith, David A. Hostutler, and Gordon D. Hager^{a)}

*Air Force Research Laboratory/Directed Energy Directorate,
Kirtland Air Force Base, New Mexico 87117-5776*

Michael C. Heaven

Department of Chemistry, Emory University, Atlanta, Georgia 30322

George C. McBane

Department of Chemistry, Grand Valley State University, Allendale, Michigan 49401

(Received 8 September 2003; accepted 6 November 2003)

An extensive data set of 54 time-resolved pump-probe measurements was used to examine CO+He rotational energy transfer within the CO $v=2$ rotational manifold. Rotational levels in the range $J_i=2-9$ were excited and collisional energy transfer of population to the levels $J_f=1-10$ was monitored. The resulting data set was analyzed by fitting to numerical solutions of the master equation. State-to-state rate constant matrices were generated using fitting law functions and *ab initio* theoretical calculations that employed the SAPT potential energy surface of Heijmen *et al.* [J. Chem. Phys. **107**, 9921 (1997)]. Fitting laws based on the modified exponential gap (MEG), statistical power exponential gap (SPEG), and energy corrected sudden with exponential power (ECS-EP) models all yielded acceptable simulations of the kinetic data, as did the theoretical rate constants. However, the latter were unique in their ability to reproduce both our kinetic data and the pressure broadening coefficients for CO+He. These results provide an impressive demonstration of the quality of the symmetry adapted perturbation theory (SAPT) potential energy surface. © 2004 American Institute of Physics. [DOI: 10.1063/1.1637341]

I. INTRODUCTION

CO–He collisions have served as a prototype for atom–diatom interactions for years. A few applications for accurate CO–He data exist, particularly in astrophysics, but the steady interest has mainly arisen from the accessibility of CO–He interactions to both experimental and theoretical studies. The atoms are small enough that theoretical descriptions both of the intermolecular forces and of the resulting collision dynamics can be nearly of quantitative accuracy. CO and He are stable and easy to handle in the laboratory, and CO can be probed by almost every popular form of state-selective spectroscopy as well as by mass spectrometry. Detailed reviews of CO–He work have appeared in papers by Thachuk *et al.*,¹ Heck and Dickinson,² Antonova *et al.*,³ and Gianturco *et al.*⁴ and therefore we will only give a brief overview here.

Experiments carried out before 1994 on He–CO gas mixtures included measurements of transport properties, virial coefficients, and pressure broadening coefficients.^{5–7} Molecular beam experiments included total cross section,⁸ differential cross section,^{9,10} relative total energy transfer cross section,¹¹ and free jet rotational relaxation measurements.^{12,13} This collection of data provided a modest

amount of information about both the attractive and repulsive parts of the potential.

In 1980, an *ab initio* potential energy surface was published by Thomas, Kraemer, and Dierksen¹⁴ (TKD) that agreed reasonably well with the experimental data available at the time. In 1994 McKellar and Chan published a high-resolution infrared spectrum of the He–CO van der Waals complex.¹⁵ Their experiment was later extended in both the IR¹⁶ and microwave^{17–19} regions. The spectroscopic data made it clear that the TKD description of the He–CO attractive well was inadequate. These results inspired a series of new theoretical efforts; at least six He–CO potential functions have been published since 1994.^{20–27} The most widely used have been the XC(fit) empirical potential of Le Roy and co-workers,²⁵ which began with a simple *ab initio* form and was adjusted to fit the infrared data, and the symmetry adapted perturbation theory (SAPT) *ab initio* potential of Heijmen *et al.*²² The XC(fit) potential gives a better description of the attractive well, though Antonova *et al.*³ suggested that the SAPT potential describes the repulsive wall more accurately on the basis of state-to-state integral cross-section measurements.

In the present work we have recorded room temperature CO–He rotational relaxation data for the first time using IR double resonance.²⁸ In these experiments a particular CO rotational state in $v=2$ is prepared by (2-0) overtone band absorption of a “pump” photon, and the subsequent collision induced populations in other rotational levels of $v=2$ are

^{a)}Author to whom correspondence should be addressed. Electronic mail: gordon.hager@kirtland.af.mil

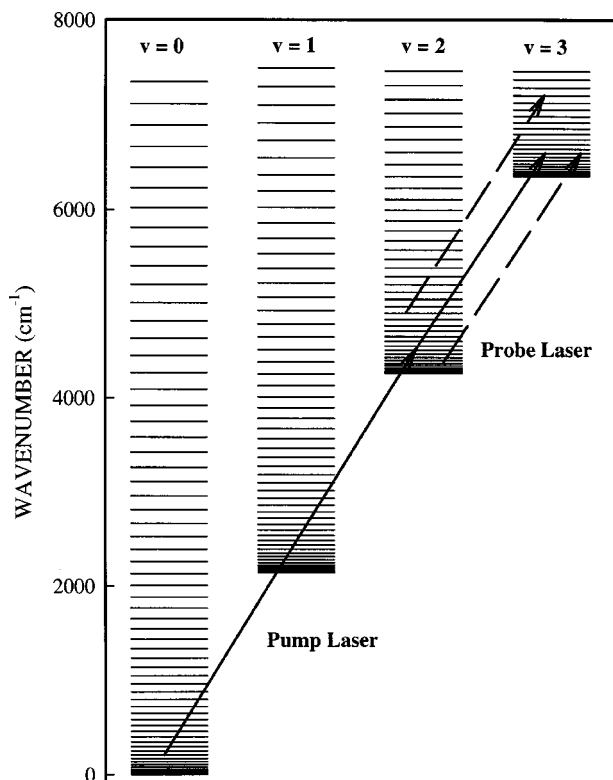


FIG. 1. An energy level diagram for the pump-probe transition scheme used in the CO IR double resonance experiment.

determined by absorption of a “probe” photon in the (3-2) band. The data set contains 54 IR double resonance pump-probe combinations. The data set, while extensive, is insufficient to determine the complete rotational energy transfer rate coefficient matrix, which has about 450 independent parameters. The full rate coefficient matrix was approximated from computer simulations of our data using the master equation and three common scaling laws: the modified exponential gap (MEG), statistical power exponential gap (SPEG), and energy corrected sudden with exponential power (ECS-EP) models. In addition, we compare the data to rate constants calculated from the SAPT potential surface.

II. EXPERIMENT

The lowest rotational and vibrational energy levels of carbon monoxide along with the IR pump-probe double resonance scheme are illustrated in Fig. 1. The pump laser pulse, represented by the long solid arrow, corresponds to excitation of a single rovibrational transition of the first overtone (2-0) band. Because the vibrational frequency ($\omega_e = 2170 \text{ cm}^{-1}$)²⁹ of CO is large, the $v=2$ level is essentially unpopulated at room temperature. Consequently, the pump laser pulse prepares a well-defined population in one initial rotational state of $v=2$. A continuous-wave (cw) probe laser was used to monitor the time-dependent population in $v=2$ through fully resolved rotational lines of the (3-2) absorption band. The short solid arrow in Fig. 1 represents the cw probe laser, which is monitoring population in a rotational level that is directly populated by the pump laser pulse. The short

dashed arrows represent probe laser transitions that arise from rotational levels populated by rotation energy transfer (RET) processes.

Our IR pump-probe double resonance experimental apparatus has been described in detail elsewhere³⁰ and only a short description will be given here. During the experiment, 0.25 Torr of CO (Air Products, ultra-high purity) and 0.50 Torr helium (Spectra Gases, ultra-high purity) were added to a 71 cm long stainless steel absorption cell. The absorption cell contained wedged calcium fluoride (CaF_2) windows and had a clear aperture diameter of 6 cm. A capacitance manometer (MKS, Baratron 622A02TBE) and a K-type thermocouple were used to monitor the pressure and temperature of the gas mixture contained within the absorption cell. The gas mixture was replaced often during the experiment to ensure that the purity remained high.

The pump laser was a pulsed optical parametric oscillator (OPO), tunable between 2.29 and 2.44 μm , described in detail elsewhere.³⁰⁻³² An injection-seeded Nd:YAG laser (Spectra-Physics, GCR 170-10) with a 6 ns pulse width operating at 10 Hz provided 130 mJ of 1064 nm radiation for the OPO. The OPO output beam had a sub-Doppler bandwidth (~ 165 MHz), a temporal pulse width of less than 6 ns, and an average pulse power of 1 mJ. To reduce the single pass gain in the absorption cell, the OPO laser beam was expanded from 3.4 to 16 mm in diameter. During the experiment, the OPO was tuned and fixed to a selected rovibrational transition of the first overtone (2-0) band and the output beam made a single pass down the center of the CO absorption cell. A small percentage of the pump laser beam was aligned through a reference cell, which contained 30 Torr of CO. A sharp decrease in transmittance was observed as the OPO laser was tuned onto the line center of a CO absorption feature. The transmittance was monitored during each experiment and data collection was terminated if the laser frequency began to drift away from the line center.

The probe laser was a narrow bandwidth (~ 30 MHz) cw lead salt diode laser (Muetek, GMBH OLS-150) tunable from 4.5 to 5.0 μm with an average power of 1 mW. The output beam was passed twice through the CO absorption cell with the incoming and outgoing beams slightly off-axis. The intensity of the probe laser was monitored with a liquid nitrogen cooled InSb detector (Kolmer Technologies, KISDP-0.5-J1, 10 ns rise time and a 12 kV/W sensitivity). The InSb detector was sensitive to both the probe and pump laser wavelengths so long pass filters were placed in front of the detector to absorb the pump radiation. The output wavelength of the probe laser was tuned by changing the temperature and current across the liquid nitrogen cooled laser diode. Unfortunately, the temperature and current setting needed to bring the diode laser wavelength resonant with a desired CO absorption feature was found to change daily. Therefore, a 0.3 m monochromator (McPherson, 218 with 150 lines/mm grating blazed at 4.0 μm) was used to confirm that the desired (3-2) band transition was being probed. The probe laser transmittance data was collected at 50 Ω input impedance on an oscilloscope, digitized, and recorded on an IBM compatible computer. To improve the signal-to-noise ratio of the

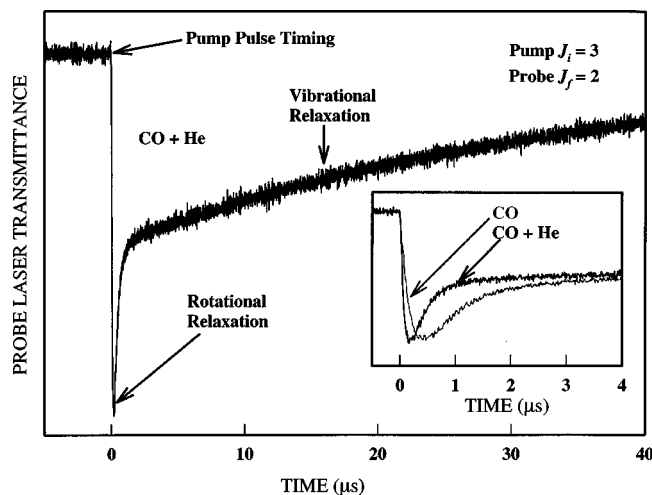


FIG. 2. A pump-probe infrared double resonance signal that displays the time-dependent transmittance of a probe laser that was tuned to the R(2) transition of the (3-2) band of CO. A sharp decrease in the cw probe transmittance occurs following the pump laser pulse. For this trace the pump was tuned to the R(2) transition of the (2-0) overtone band. The double resonance signal displays rapid rotational relaxation at early times while vibrational loss from $v=2$ is responsible for the long exponential decay. The inset is an expanded region of the double resonance signal. The gray trace in the inset is the double resonance signal for 0.25 Torr of CO and the black trace is the signal for 0.25 Torr of CO and 0.5 Torr of He.

collected double resonance data the oscilloscope was set to average 100 traces.

Both the pump and probe lasers were linearly polarized and care was taken to ensure that the data did not incur error from initial state alignments. The polarization effects were completely avoided in our double resonance data by setting the pump and probe laser polarization alignment to the magic angle (54.74°).

III. RESULTS

A typical IR double resonance signal is displayed in Fig. 2, which shows the time-dependent relative transmittance of the probe laser. In Fig. 2, the pump laser was resonant with the R(2) branch transition of the first overtone (2-0) band of CO, pumping $J_i=3$ of $v=2$, while the probe laser was tuned to the R(2) branch transition of the (3-2) band, monitoring the population in $J_f=2$ of $v=2$. The background thermal population in $v=2$ of room temperature CO is negligible and the transmittance of the probe laser through the CO absorption cell was a maximum value before the pump laser fired. The pump laser prepared population in a single quantum state ($J_i=3$ of $v=2$) at $t=0$ and collisions immediately began to redistribute population among the neighboring rotational levels, producing a sharp decrease of the probe laser transmittance following $t=0$. The long exponential decay in the IR double resonance data is due to the vibrational relaxation process as CO molecules are removed from $v=2$. Information about the rotational relaxation process is contained in the initial spiked feature in the IR double resonance data. The inset in Fig. 2 displays an expansion of the initial IR double resonance data on a faster time scale. The gray trace shows the experimental IR double resonance data for only 0.25 Torr of pure CO while the black trace displays the IR

double resonance data for a mixture of 0.25 Torr of CO and 0.50 Torr of helium. It is clear from the inset in Fig. 2 that the addition of helium increases the rate at which the rotational relaxation process occurs.

A. Data reduction

We have collected an extensive data set that contains 54 IR double resonance pump-probe combinations. During the experiment both the pump and probe lasers were tuned to the line centers of each CO transition and the pump-probe data was collected at 10 ns time steps resulting in 501 data points between -1 and $4 \mu\text{s}$ (similar to the data shown in the inset in Fig. 2). Our IR double resonance data reduction method was described in detail in our previous paper on CO self-rotational relaxation and only a brief description will be given here.³⁰ The ideal data for a straightforward study of CO-He RT rate processes would only contain RET information. However, it is easily seen from Fig. 2 that the double resonance data is a composite of both rotational and vibrational energy transfer processes. The rapidly changing part of the signal in the $0-3 \mu\text{s}$ range results from the rotational relaxation process. After $3 \mu\text{s}$ the rotational distribution reaches equilibrium and the slow decay is determined by vibrational relaxation. There is an additional complication that arises from velocity changing collisions. The pump laser (165 MHz linewidth) excited a velocity subgroup within the 300 MHz wide Doppler profile of the CO rotational line. Velocity relaxation then caused a time-dependent broadening of the probe transitions, which contributed to the decay of the probe laser absorption signal monitored at the line center. In order to correct for velocity relaxation effects we needed to characterize the time-dependent evolution of the lineshape of the probe transition. This was accomplished by collecting time-resolved double resonance data at fixed frequencies, while stepping the probe laser across the absorption profile of the CO transition. These series of time-resolved double resonance traces were transformed to frequency-resolved linewidth measurements at every time step. An analytical expression that could be used to parametrize the lineshape data was then constructed by the following procedure. At each time step the frequency-resolved linewidth data was fit with a Gaussian function and the CO transition linewidth was determined (see the data displayed in the inset of Fig. 3). The resulting measured time-dependent linewidth data had a sigmoid shape. The sigmoid function

$$\Delta\nu(t) = a_1 + \frac{b_1}{1 + \exp(-(t - c_1)/d_1)} \quad (1)$$

was found to represent the time-dependent linewidth data very well, where a_1 , b_1 , c_1 , and d_1 are adjustable fitting parameters (the subscript for each adjustable fitting parameter was chosen to coincide with the equation number). The gray trace through the center of the measured linewidth data in Fig. 3 represents a fit of the linewidth data using Eq. (1).

The CO-He RET contribution to the IR double resonance data was extracted by first correcting for the effects of vibrational relaxation. Since the number density of CO($v=2$) prepared by the weak pump laser pulse was very low, the most probable collisions for CO($v=2$) occurred with the

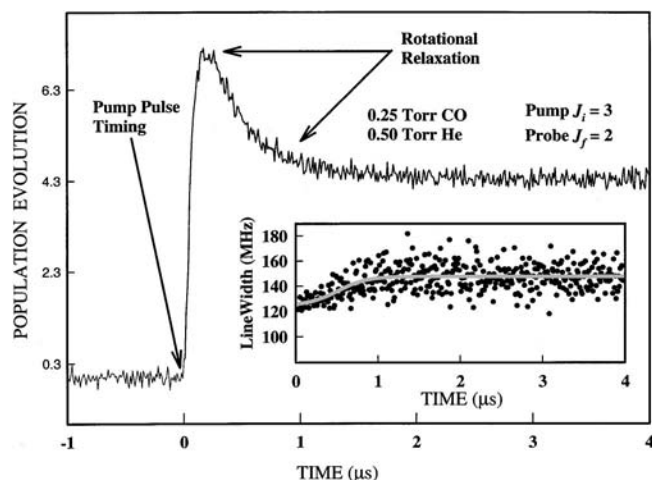


FIG. 3. The time-dependent rotational population evolution for $J_f=2$ after excitation of $J_i=3$. The inset shows the experimentally determined time-dependent excited state linewidths (in MHz) for the $J_f=2$ level following excitation of $J_i=3$. The experimental data are represented by dots while the line through the center of the data is a fit of the time-dependent linewidth using Eq. (1).

higher number density CO($v=0$) and He collision partners. The rate for vibrational-to-vibrational (VV) relaxation,³³ $\text{CO}(v=2) + \text{CO}(v=0) \rightarrow 2 \text{CO}(v=1)$, is $\sim k_{VV} = 2.73 \times 10^{-12} \text{ cm}^3 \text{ molecule}^{-1} \text{ s}^{-1}$. Since the vibrational-to-translational (VT) relaxation of CO($v=2$) by CO($v=0$) and He are much slower, the vibrational relaxation of CO($v=2$) was dominated by CO VV self-relaxation. The double resonance data was corrected for vibrational relaxation by the simple transformation

$$F(J_i, J_f, t) = -f(J_i, J_f, t) \exp(k_{VV} M t), \quad (2)$$

where $f(J_i, J_f, t)$ is the experimental double resonance signal for pumping J_i and probing J_f , M is the number density

$$\bar{P}(J_i, J_f, t) = a_4 \left[1 - \exp(-b_4 t) - \frac{c_4}{c_4 + d_4} \left(1 + \frac{b_4 \exp(-(c_4 + d_4)t) - (c_4 + d_4) \exp(-b_4 t)}{c_4 + d_4 - b_4} \right) \right], \quad (4)$$

where a_4 , b_4 , c_4 , and d_4 are adjustable fitting parameters. This expression accurately reproduced the population evolutions. The fitted parameters for Eq. (4) are collected in Table I.

Rotational relaxation in $v=2$ was simulated using the series of coupled differential equations (the master equation) defined by

$$\begin{aligned} \frac{dN_J}{dt} = & \sum_{J'} (k_{J \leftarrow J'}^{\text{CO-CO}} N_{J'} - k_{J' \leftarrow J}^{\text{CO-CO}} N_J) [\text{CO}] \\ & + \sum_{J'} (k_{J \leftarrow J'}^{\text{CO-He}} N_{J'} - k_{J' \leftarrow J}^{\text{CO-He}} N_J) [\text{He}], \end{aligned} \quad (5)$$

where N_J is the population in rotational level J , and $k_{J \leftarrow J'}^{\text{CO-CO}}$ and $k_{J \leftarrow J'}^{\text{CO-He}}$ are CO-CO and CO-He relaxation rate con-

stants for transfer from J' to J , respectively. During the experiment RET arises from both CO-CO and CO-He interactions and Eq. (5) accounts for both kinetic processes. Since our primary object for this work was to study CO-He RET the CO-CO rotational relaxation rate constants ($k_{J \leftarrow J'}^{\text{CO-CO}}$) were taken from the work of Phipps *et al.*³⁰ The master equation, as written in Eq. (5), incorporates all rotational levels. However, only those rotational levels that contain significant thermal populations need to be included to provide an accurate description of rotational relaxation. Since $\sim 97\%$ of the rotational population resides in rotational levels below $J < 20$ at 297 K we restricted the model to consider $J \leq 29$. A matrix of 900 rate constants is needed to solve this system of equations. Applying detailed balance and setting the diagonal elastic rates to zero reduces the problem to that of finding

$$P(J_i, J_f, t) = F(J_i, J_f, t) \frac{\Delta v(t)}{\Delta v(0)}. \quad (3)$$

Figure 3 shows a plot of a typical time-resolved population profile that was generated from the raw data by application of Eqs. (2) and (3). Note that the trace converges to a constant value beyond 2 μs , indicating the rotational equilibrium has been reached and the effects of vibrational relaxation have been successfully taken into account.

B. Computer simulation of rotational relaxation kinetics

At rotational equilibrium the populations of the rotational levels conform to a Boltzmann distribution. However, since the pump and probe laser intensities changed daily, the relative intensities of the experimental double resonance data had little meaning. This defect was overcome by scaling the average value of each population profile between 3 and 4 μs to a corresponding Boltzmann percentage. For example, at rotational equilibrium $J=2$ has a Boltzmann population of 4.31%, so the y-axis in Fig. 3 has been scaled so that this value coincides with the data at the asymptote.

To facilitate computer simulations of the reduced data sets the time-dependent population profiles were represented by the expression

TABLE I. Coefficients for Eq. (4) which represent the time-dependent population evolutions.

J_i	J_f	a_4^a	b_4	c_4	d_4	J_i	J_f	a_4	b_4	c_4	d_4
2	3	23.1992	0.006 370	0.004 772	0.001 558	6	9	11.3785	0.005 653	0.001 874	0.003 772
2	4	14.5029	0.008 962	0.001 847	0.001 642	6	10	6.9987	0.005 733	-0.000 059	0.871 089
2	5	14.0701	0.007 434	0.001 471	0.001 735	7	1	3.7302	0.004 505	0.000 747	0.001 912
2	6	14.6149	0.004 568	0.001 863	0.002 293	7	2	5.3239	0.006 989	0.000 530	0.002 252
3	2	10.9780	0.010 944	0.002 022	0.001 307	7	3	7.4286	0.005 747	0.000 553	0.001 840
3	4	13.0418	0.011 193	0.001 523	0.001 672	7	4	9.0246	0.007 699	0.000 661	0.002 053
3	5	13.1826	0.007 952	0.001 310	0.001 792	7	5	15.0569	0.006 193	0.002 999	0.003 068
3	6	12.3222	0.006 678	0.001 255	0.002 377	7	6	13.3771	0.009 248	0.001 561	0.002 370
4	2	9.1706	0.008 412	0.001 886	0.001 672	7	8	17.7054	0.006 380	0.003 461	0.002 864
4	3	15.856	0.007 375	0.003 414	0.001 922	7	9	13.6106	0.005 547	0.002 240	0.002 834
4	5	15.0380	0.008 658	0.002 168	0.002 223	7	10	10.6333	0.006 357	0.002 183	0.004 205
4	6	12.7142	0.007 349	0.001 337	0.002 319	8	2	6.1946	0.004 041	0.001 195	0.002 733
4	8	12.3275	0.004 151	0.001 450	0.002 696	8	3	8.1089	0.004 495	0.001 224	0.002 917
5	2	8.3342	0.006 904	0.001 828	0.001 957	8	4	9.9897	0.004 453	0.001 341	0.002 894
5	3	11.1262	0.007 853	0.001 696	0.001 789	8	5	11.7693	0.005 733	0.001 957	0.003 587
5	4	11.6938	0.010 187	0.001 380	0.001 935	8	6	10.9397	0.008 022	0.000 715	0.002 004
5	6	12.7817	0.009 714	0.001 097	0.001 876	8	7	13.6824	0.009 142	0.001 712	0.002 551
5	7	12.6531	0.007 727	0.001 320	0.002 420	8	9	16.1328	0.006 805	0.003 519	0.003 135
5	8	11.5019	0.006 660	0.001 743	0.004 010	8	10	10.0127	0.007 521	0.002 213	0.005 139
5	9	9.7784	0.004 781	0.001 026	0.003 586	9	2	5.9837	0.005 246	0.051 713	0.133 115
5	10	6.9994	0.004 612	2.182e-05	0.663 534	9	3	7.6658	0.003 734	0.000 945	0.002 763
6	2	8.4103	0.004 580	0.002 231	0.002 345	9	4	6.9728	0.006 075	2.691e-05	0.001 236
6	3	7.9829	0.008 319	0.000 656	0.001 650	9	5	7.6139	0.006 326	4.327e-07	0.111 293
6	4	10.7057	0.008 391	0.001 372	0.002 414	9	6	9.3666	0.007 779	0.000 612	0.003 792
6	5	13.2719	0.009 934	0.001 503	0.002 022	9	7	15.3107	0.006 101	0.002 753	0.003 164
6	7	18.1716	0.006 698	0.003 642	0.002 986	9	8	17.5374	0.007 284	0.003 948	0.003 325
6	8	12.5916	0.007 307	0.001 974	0.003 460	9	10	15.0758	0.007 217	0.003 823	0.003 313

^aParameter has units of number density (molecules cm⁻³); sufficient digits are quoted to reproduce the original data to full accuracy.

435 independent rate constants, but this is obviously too many parameters to be determined from the data collected in these experiments. Therefore, we have applied the usual method of representing the CO–He rotational-translation relaxation rate constant matrix with fitting law functions.

The full CO–He rotational relaxation rate constant matrix was extracted using three of the most common fitting laws:³⁴ modified exponential gap (MEG), statistical power exponential gap (SPEG), and energy corrected sudden with exponential gap basis rates (ECS-EP). Please refer to our previous CO–CO RET paper for a detailed descriptions of our technique and procedure for using these fitting laws.³⁰

The master equation was solved numerically using the fourth-order Runge–Kutta method and the MEG, SPEG, and ECS-EP fitting law expressions were fitted to the $\bar{P}(J_i, J_f, t)$ curves. The variance between the observed and calculated population profiles, sampled at 100 points between 0 and 4 μ s, was minimized by iteratively changing the values of the adjustable parameters for each fitting law expression.

Good agreement between the simulations and the experimental data was achieved and the optimized fitting law parameters are listed in Table II. The estimated error was determined by adjusting each parameter, while holding the

TABLE II. Experimentally determined parameters for the MEG, SPEG, and ECS-EP fitting laws and the variance between computer simulations and our experimental data.

Parameters	Fitting results ^a				Theoretical results SAPT ^e
	MEG	SPEG	ECS-EP	ECS ^d	
α (10 ⁻¹¹ cm ³ molecules ⁻¹ s ⁻¹)	5.17(54)	12.76(1.40)	4.77(39)
b	1.36(16)	1.45(15)	0.27(12)
c	2.14(19)	0.276(29)	0.753(27)
lc (Å)	... ^b	... ^b	1.6(1.3)
σ^{2c}	0.1827	0.1860	0.1859	0.3620	0.2470

^aExperimental values from this work. Values in parentheses are estimated error which were obtained by varying the parameter until a 10% increase in the variance was obtained while holding all other parameters constant.

^bParameter not associated with the fitting law.

^cVariance between experimental and computer simulated population evolutions.

^dVariance from computer simulations of our experimental data using the ECS fitting law rate matrix of Bel Bruno *et al.* (Ref. 35).

^eVariance from computer simulations of our experimental data using a rate matrix calculated using the symmetry adapted perturbation theory (SAPT) potential energy surface (Ref. 22).

other parameters constant, until a 10% increase in the variance was observed. Surprisingly, the three fitting laws reproduced the data with nearly the same variance. The MEG law had a slightly lower variance ($\sim 2\%$ lower than the best fit variance of the SPEG and ECS-EP laws). The only literature values for the rate constants, determined from pressure broadening studies of the Raman Q-branch spectrum, were obtained by BelBruno *et al.*³⁵ using the ECS fitting law. These authors used a slightly different expression to represent the ECS basis rate constants ($k_{J \leftarrow 0}^{\text{CO-He}}$) from the one used in our analysis and therefore our fitted parameters are not directly comparable with theirs. However, we have used their relaxation rate constant matrix to simulate our data and the variance from this calculation is listed in Table II. This rate constant set yields population profiles that deviate significantly from the experimental results. The largest discrepancies occur for processes that involve small changes in the angular momentum.

C. Theoretical calculations

A rate coefficient matrix was calculated directly from the SAPT *ab initio* potential surface of Heijmen *et al.*²² Time-independent scattering calculations were used to evaluate state-to-state collision cross sections for the rotationally inelastic processes, and these cross sections were then averaged over the distribution of collision energies to obtain rate coefficients. Details of the calculations are described in the following paragraphs.

1. Scattering calculations

Although the SAPT potential includes the vibrational coordinate of CO, the present scattering calculations were simplified by treating CO as a rigid rotor. A two-dimensional intermolecular potential was derived from the full SAPT potential by averaging over the CO vibrational motion. The expectation values of the CO internuclear distance, $\langle \Phi_2(r) | r^n | \Phi_2(r) \rangle$, where $\Phi_2(r)$ is the $v=2$ vibrational wavefunction, were needed for construction of the vibrationally averaged potential. These matrix elements were calculated with the LEVEL program of Le Roy.³⁶ The two-dimensional potential was expanded in terms of Legendre polynomials with radially dependent expansion coefficients (the standard VRTP representation of MOLSCAT). For energies up to 870 cm^{-1} a 12 term expansion was used. The number of polynomials was increased to 18 for the higher energy region of the potential.

The MOLSCAT program of Hutson and Green³⁷ was used for all the scattering calculations. The close coupled equations were solved using the hybrid log derivative Airy propagator of Alexander and Manolopolous.³⁸ The energies of the asymptotic $v=2$ CO rotational levels were calculated from the molecular constants of Maki, Wells, and Jennings.³⁹ The rotational basis sets contained all open channels and at least two closed channels at each energy. "Exact" close coupled (CC) calculations were performed for total energies below 870 cm^{-1} and the coupled states (CS) approximation of McGuire and Kouri⁴⁰ was used for higher energies. All propagations were carried out to a center of mass separation of at least $40a_0$, though many of the calculations were ex-

tended to larger distances to ensure that the asymptotic boundary conditions were imposed beyond the centrifugal barrier. The partial wave sum was terminated when the elastic cross sections had converged to at least 1 \AA^2 and the inelastic cross sections to 0.005 \AA^2 .

The most rapid variations in the inelastic cross sections with collision energy occur at very low collision energies, and just above the energy thresholds for opening of new asymptotic channels. The grid of energies used in the calculations was selected to capture most of those variations for the subsequent thermal average. Just above each threshold, beginning with $J=1$, a series of total energies was used whose spacings began at 1 cm^{-1} and increased to larger values as the cross sections became smoother. Each series was terminated when the next threshold was reached. For all thresholds below $J=21$, CC calculations up to kinetic energies of about $4kT$ were performed. Beginning at the $J=21$ threshold (870.7 cm^{-1}), CS calculations were used and the total energies extended up to 2500 cm^{-1} .

2. Thermal averaging

Thermally averaged cross sections were evaluated according to the expression

$$\sigma_{if}(T) = (kT)^{-2} \int_0^\infty \varepsilon_t \sigma_{if}(\varepsilon_t) \exp(-\varepsilon_t/kT) d\varepsilon_t, \quad (6)$$

where ε_t is the precollision center-of-mass translational energy. The integration average was carried out using trapezoidal rule for $\varepsilon_t \leq 2500 \text{ cm}^{-1}$. Beyond this range the integral was evaluated analytically by assuming that the cross section $\sigma_{if}(\varepsilon_t)$ was independent of the collision energy.

Cross sections for upward and downward transitions between two rotational states should obey the principle of detailed balance for both the CC and CS cross sections. We therefore checked our thermalized cross sections for consistency with detailed balance as a means of evaluating the accuracy of the Boltzmann averaging procedure, and in particular the effect of our assumption of constant cross sections for translational energies above 2500 cm^{-1} . For each pair of CO levels, we evaluated a "fractional detailed balance error," ε_{db} , from

$$\varepsilon_{db} = \left(\sigma_{if}(T) - \sigma_{fi}(T) \frac{2J_f + 1}{2J_i + 1} \times \exp(-(\varepsilon_f - \varepsilon_i)/kT) \right) / \sigma_{if}(T). \quad (7)$$

No transition involving $J \leq 24$ levels showed a fractional error greater than 1%. Errors of 10% appeared above $J=30$. Because more than 97% of the equilibrium CO population is in $J < 20$ at 297 K, the errors in the thermalized cross sections involving high J should be unimportant in comparisons with the data. The thermalized cross sections were multiplied by the average collision speed, $\langle v \rangle = (8kT/\pi\mu)^{1/2}$ ($1.34 \times 10^3 \text{ m s}^{-1}$), to convert them to state-to-state rate coefficients.

The *ab initio* rate constants were used to simulate the $P(J_i, J_f, t)$ data. Figures 4–8 show comparisons of the experimental and simulated curves. In each of the figures the

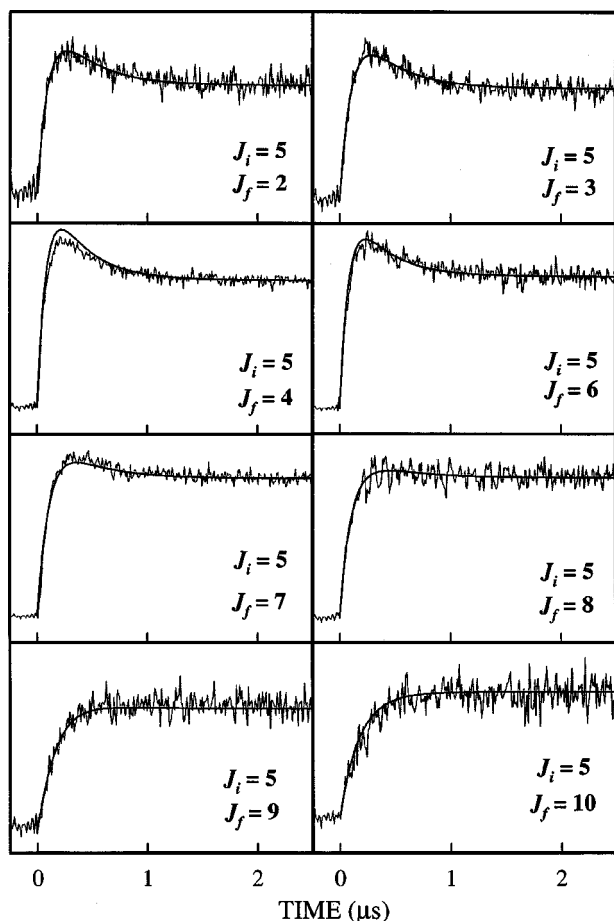


FIG. 4. Time-dependent rotational populations for $J_f=2-10$, with the exception of $J_f=5$, following the excitation of $J_i=5$. The smooth lines through the data are from computer simulations that used rate constants derived from the SAPT potential energy surface (Ref. 22).

simulated populations are represented by the smooth curves through the $P(J_i, J_f, t)$ data. To illustrate the quality of the fit for levels with small equilibrium populations, the data in Figs. 4–8 are not all displayed on the same relative intensity scale. The agreement between the SAPT theoretical rate matrix model and the experimental data was very favorable, with most of the simulations lying within the noise limits of the experimental data.

IV. DISCUSSION

Graphical representations of the rate constant matrices from the MPEG, SPEG, ECS-EP, and SAPT models are shown in Fig. 9. As all four models provide reasonably good simulations, it is evident that the data do not define a unique set of rate constants. Careful inspection of the matrices shows that they are fairly similar for the rate constants that determine transfer between the levels ($J_i=5-10$, $J_f=5-10$). The most obvious discrepancies are for the rate constants associated with high values of $J_i (>15)$. The high- J_i regions of the rate constant matrices can be assessed by considering the pressure broadening data for He+CO, as this data extends up to $J_i=21$. Approximate pressure broadening coefficients were calculated by assuming that RET is the

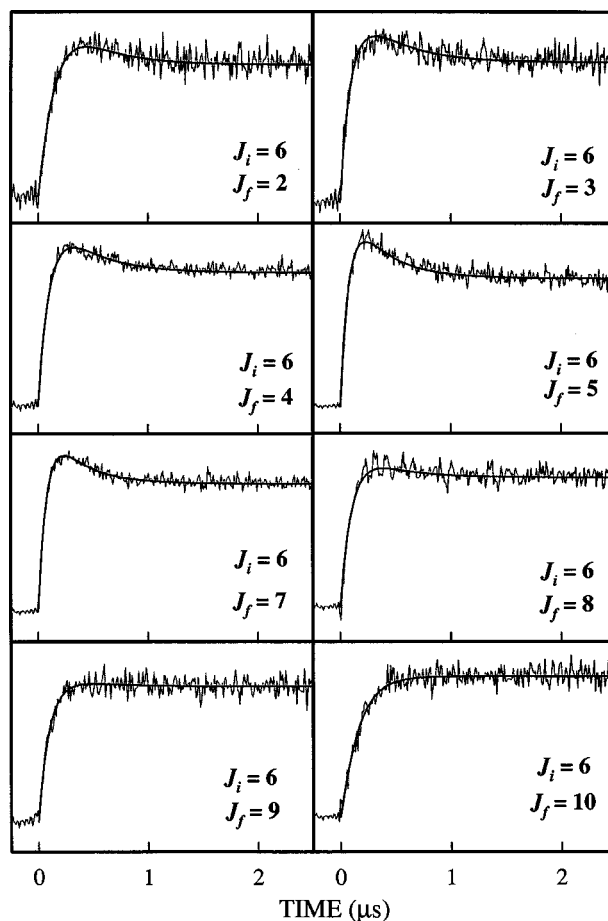


FIG. 5. Time-dependent rotational populations for $J_f=2-10$, with the exception of $J_f=6$, following the excitation of $J_i=6$. The smooth lines through the data are from computer simulations that used rate constants derived from the SAPT potential energy surface (Ref. 22).

dominant collision process and that the RET rate constant matrices are the same for the $v=0$ and 2 levels. The pressure broadening coefficients are then given by⁴¹

$$\gamma(J', J'') = \frac{1}{4\pi} \left(\sum_{J'_f} k_{J'_f \leftarrow J'} + \sum_{J''_f} k_{J''_f \leftarrow J''} \right), \quad (8)$$

where J' and J'' are the upper and lower J values for a specific rovibrational line. Pressure broadening coefficients calculated from the rate constant matrices are compared with the experimental data of BelBruno *et al.*⁴² in Fig. 10. Here it can be seen that the rate constants derived from the SAPT potential energy surface perform far better than those from the present fitting-law expressions. The reason why our fitting-law rate constants fail this test is easily discerned from the plots in Fig. 9. The rate constants for removal of population from a given rotational level ($k_{J_i}^T = \sum_{J_f} k_{J_f \leftarrow J_i}$) decrease with increasing J_i because the fitting-law expressions decrease as the energy gaps between the levels increases. This results in a predicted drop in the pressure broadening coefficients with increasing J_i . The ECS model of BelBruno *et al.*³³ reproduced the pressure broadening data by using parameters that yielded a very weak dependence on the energy gaps. Consequently, their rate constants for transitions with large values of $|\Delta E|$ (and $|\Delta J|$) were relatively large.

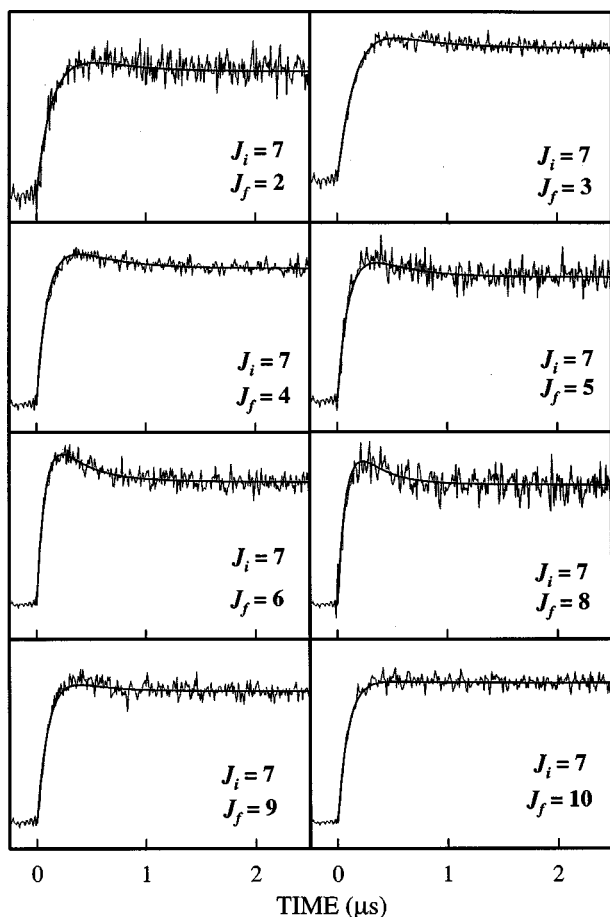


FIG. 6. Time-dependent rotational population evolutions for $J_f=2-10$, with the exception of $J_f=7$, following the excitation of $J_i=7$. The smooth lines through the data are from computer simulations that used rate constants derived from the SAPT potential energy surface (Ref. 22).

Because their $k_{J_i}^T$ summations were limited by the pressure broadening coefficients, their state-to-state rate constants for small $|\Delta J|$ transitions were constrained to be relatively low. The low rate constants for small $|\Delta J|$ transitions were reflected in the kinetic simulations of our double resonance data, where the temporal population profiles for levels adjacent to J_i were in poor agreement with the measurements.

Rate constants from the SAPT potential reproduced both the kinetic and pressure broadening data. This model succeeds because the $k_{J_i}^T$ rate constants are nearly constant with increasing J_i (for $J_i > 5$), as there is very little dependence on the energy gaps for the transitions that dominate the rate constant matrix. The dependence of the rate constants on $|\Delta J|$ is more consistent with an energy transfer process that is governed by the momentum gap.

The rate constant matrix derived from the theoretical calculations is presented in Table III. For transitions with small to moderate values of $|\Delta J|$ the rate constants show a preference for transitions with odd values of ΔJ . This trend is illustrated in Fig. 11 where the rate constants for transfer from $J_i=5$ and 10 are plotted as a function of J_f . Antonova *et al.*³ observed this symmetry preference in their crossed-beam study of He+CO rotationally inelastic scattering. Two collision energies were examined (583 and 720 cm^{-1}) and in

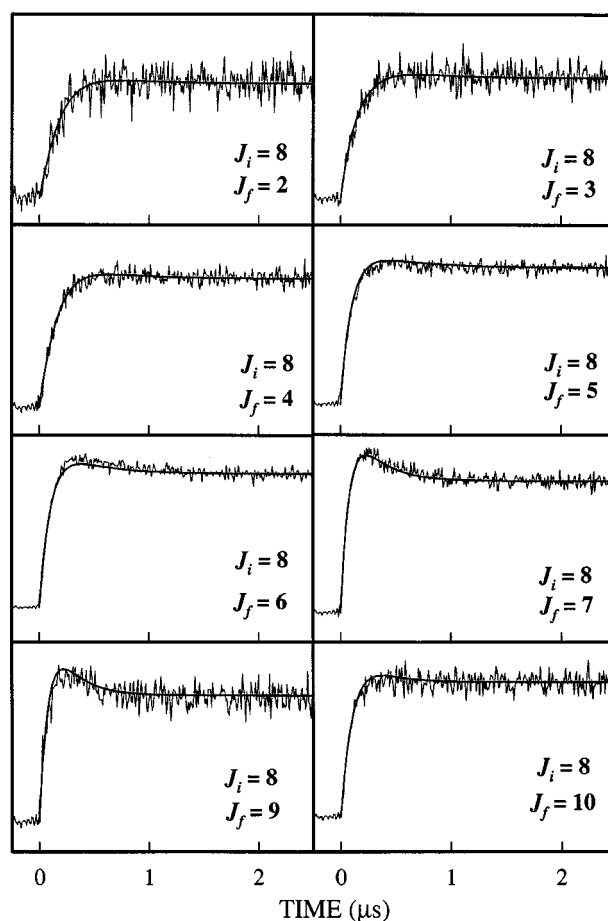


FIG. 7. Time-dependent rotational population evolutions for $J_f=2-10$, with the exception of $J_f=8$, following the excitation of $J_i=8$. The smooth lines through the data are from computer simulations that used rate constants derived from the SAPT potential energy surface (Ref. 22).

both instances the CO final state distributions showed a clear preference for odd ΔJ transitions. Antonova *et al.*³ found that cross sections calculated from the SAPT potential also exhibited this trend. The fact that the propensity for odd ΔJ transitions is manifest by the calculated rate constants indicates that the SAPT potential produces this effect for a broad range of collision energies. Unfortunately, the data from the present study cannot be used to test this aspect of the theoretical model. The raw experimental observations did not show a symmetry preference. In part this was due to the fact that both CO+CO and CO+He collisions contribute to the transfer process. As the former has a preference for even ΔJ transitions the combination with CO+He events that favor odd ΔJ diminishes the degree of modulation observed. There is some compensation for this interference in the data analysis as the kinetic model included the symmetry preference of the CO+CO collisions. However, the latitude in fitting the He+CO rate constants was such that the existence of a symmetry preference could not be established meaningfully according to the statistics of the fitting procedure.

In their study of CO+CO collisions, Phipps *et al.*³⁰ found an interesting correlation between the rotational energy transferred and the degree of velocity randomization for single collision events. Collisions that exchanged small quantities of rotational energy were ineffective in relaxing

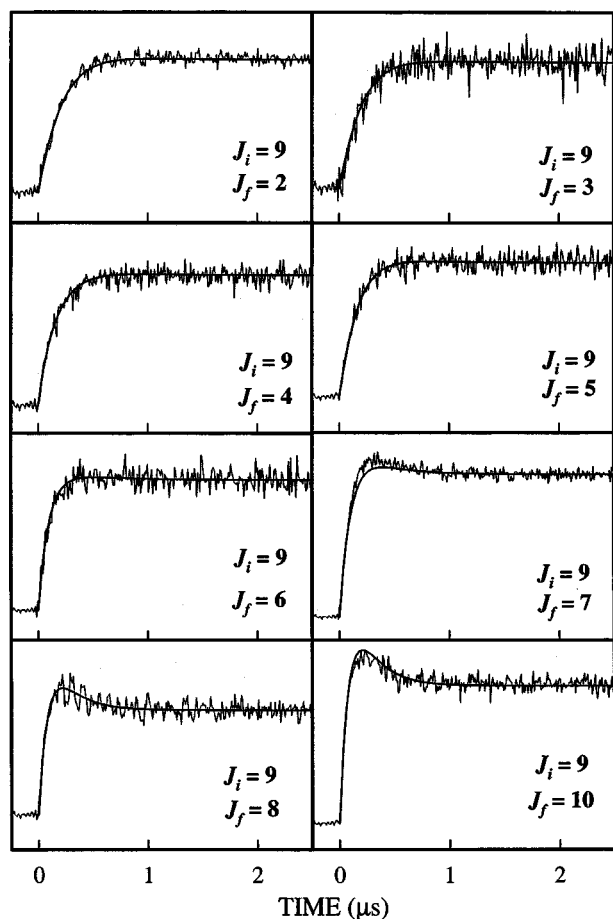


FIG. 8. Time-dependent rotational population evolutions for $J_f=2-10$, with the exception of $J_f=9$, following the excitation of $J_i=9$. The smooth lines through the data are from computer simulations that used rate constants derived from the SAPT potential energy surface (Ref. 22).

the velocity distribution. Conversely, collisions that caused large changes in the rotational energy were also effective in randomizing the velocities. This trend indicated that small ΔE transitions were mediated by long-range attractive forces while a much harder collision, involving the repulsive wall of the intermolecular potential, was needed to impart large rotational energy changes. This behavior was much less apparent for CO+He. The linewidth measurements indicated that all single-collision transitions were highly effective at velocity randomization. This was to be expected as the long-range attractive forces between CO and He are too weak to be efficient in mediating energy transfer. Even for small ΔJ transitions, energy transfer is an impulsive event that occurs on the repulsive wall of the potential.

V. SUMMARY

Time-resolved pump-probe measurements were used to examine CO+He rotational energy transfer within the CO $v=2$ rotational manifold. Rotational levels in the range $J_i=2-9$ were excited and transfer of population to the levels $J_f=1-10$ was monitored. The resulting data set was analyzed by fitting to numerical solutions of the master equation. State-to-state rate constant matrices were generated using fitting law functions and *ab initio* theoretical calculations

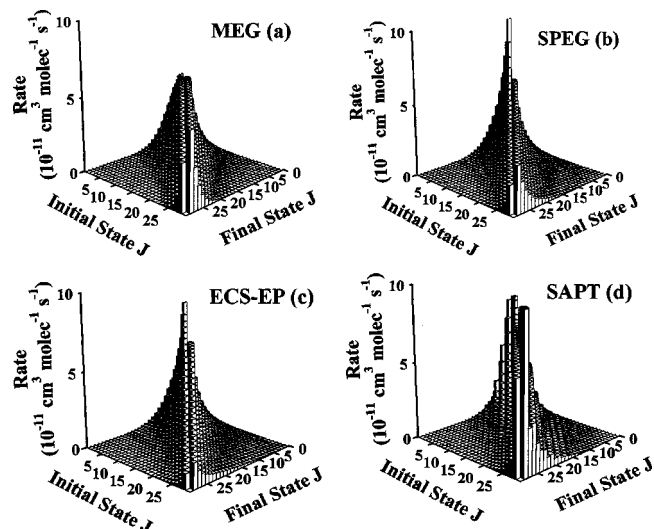


FIG. 9. Bar graph representations of the best fit rate constant matrices generated from the MEG, SPEG, and ECS-EP models are displayed in plots *a*, *b*, and *c*, respectively. Rate constants predicted from the SAPT potential energy surface are displayed in plot *d*.

that employed the SAPT potential energy surface.²² Fitting laws based on the MEG, SPEG, and ECS-EP models all yielded acceptable simulations of the kinetic data, as did the theoretical rate constants. However, the latter were found to be unique in their ability to reproduce both the kinetic data and the pressure broadening coefficients for CO+He. These results provide an impressive demonstration of the quality of the SAPT potential energy surface.

The fitting law expressions were unable to reproduce the combined kinetic and pressure broadening data because the rate constants were primarily dependent on the transition energy gaps in these models. The pronounced fall-off in the

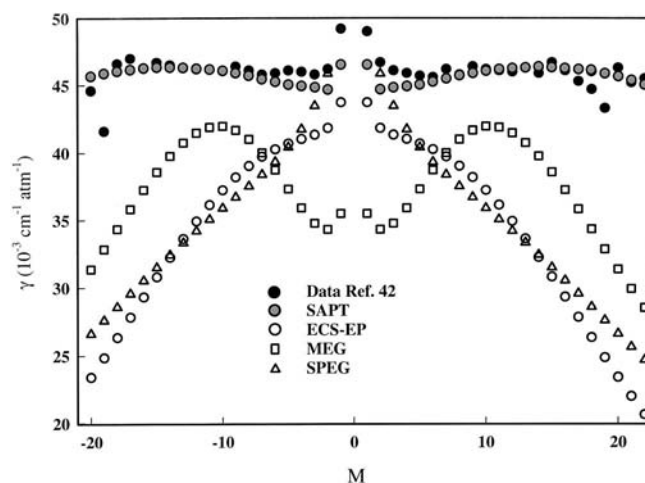


FIG. 10. Simulations of the CO-He pressure broadening data using the predictions for the SAPT potential energy surface, and the ECS-EP, MEG, and SPEG fitting law models. Negative values of the index M correspond to P branch lines with $J=-M$. Positive values of M indicate R branch lines with $J=M-1$. The experimental CO-He pressure broadening data were taken from Ref. 40 and are illustrated by the solid black circles. The predictions from the SAPT PES are represented by gray solid circles, the ECS-EP fitting law by open circles, and the MEG and SPEG fitting laws are represented by open squares and triangles, respectively.

TABLE III. Theoretical CO+He inelastic rotational relaxation rate constants calculated from the SAPT PES. Rate constants in units of $10^{-11} \text{ cm}^3 \text{ molecule}^{-1} \text{ s}^{-1}$.

$J_i \backslash J_f$	0	1	2	3	4	5	6	7	8	9	10	11	12	13	14	15	16	17	18	19	20
0	0	2.40	1.54	1.27	0.31	0.57	0.17	0.25	0.13	0.10	0.08	0.05	0.05	0.03	0.03	0.02	0.01	0.01	0.01	0.01	0
1	7.07	0	5.10	2.53	2.65	0.70	1.20	0.43	0.51	0.31	0.22	0.20	0.11	0.11	0.06	0.06	0.04	0.03	0.02	0.02	0.01
2	7.28	8.20	0	6.02	3.01	3.25	0.96	1.49	0.61	0.65	0.43	0.29	0.26	0.15	0.15	0.09	0.08	0.05	0.04	0.03	0.02
3	7.97	5.39	7.97	0	6.31	3.32	3.53	1.11	1.66	0.71	0.74	0.49	0.34	0.31	0.18	0.18	0.11	0.10	0.07	0.05	0.04
4	2.34	6.74	4.76	7.54	0	6.40	3.49	3.72	1.19	1.79	0.77	0.81	0.55	0.37	0.35	0.20	0.20	0.12	0.11	0.08	0.06
5	4.76	1.97	5.75	4.43	7.13	0	6.49	3.55	3.87	1.24	1.89	0.82	0.86	0.59	0.40	0.38	0.22	0.22	0.14	0.12	0.09
6	1.48	3.62	1.79	4.98	4.12	6.88	0	6.63	3.57	3.99	1.27	1.96	0.86	0.90	0.63	0.43	0.41	0.24	0.24	0.15	0.14
7	2.24	1.32	2.82	1.59	4.46	3.82	6.73	0	6.78	3.56	4.09	1.30	2.01	0.90	0.93	0.67	0.45	0.44	0.25	0.26	0.16
8	1.11	1.53	1.13	2.33	1.40	4.08	3.55	6.64	0	6.95	3.53	4.16	1.33	2.05	0.95	0.95	0.70	0.47	0.46	0.27	0.27
9	0.82	0.89	1.15	0.94	1.99	1.23	3.76	3.30	6.59	0	7.12	3.50	4.22	1.37	2.07	0.99	0.96	0.74	0.48	0.48	0.28
10	0.64	0.56	0.69	0.91	0.79	1.73	1.10	3.50	3.08	6.56	0	7.31	3.46	4.25	1.40	2.08	1.03	0.96	0.77	0.49	0.50
11	0.32	0.46	0.42	0.54	0.75	0.67	1.52	1.00	3.26	2.89	6.55	0	7.49	3.42	4.27	1.43	2.08	1.07	0.96	0.80	0.49
12	0.29	0.22	0.34	0.32	0.44	0.62	0.58	1.35	0.91	3.04	2.71	6.54	0	7.67	3.37	4.28	1.46	2.06	1.11	0.94	0.82
13	0.13	0.19	0.16	0.25	0.26	0.36	0.52	0.51	1.19	0.84	2.83	2.54	6.54	0	7.86	3.31	4.27	1.49	2.01	1.15	0.92
14	0.11	0.09	0.13	0.12	0.20	0.21	0.30	0.44	0.46	1.06	0.78	2.64	2.39	6.54	0	8.04	3.24	4.25	1.52	1.95	1.18
15	0.05	0.07	0.06	0.10	0.09	0.16	0.17	0.26	0.37	0.41	0.94	0.72	2.46	2.24	6.54	0	8.22	3.16	4.21	1.56	1.88
16	0.04	0.04	0.05	0.05	0.07	0.07	0.13	0.14	0.22	0.32	0.37	0.83	0.67	2.30	2.10	6.54	0	8.40	3.07	4.14	1.60
17	0.02	0.02	0.02	0.03	0.03	0.06	0.06	0.10	0.11	0.19	0.27	0.33	0.73	0.62	2.14	1.96	6.54	0	8.59	2.99	4.04
18	0.01	0.01	0.01	0.02	0.02	0.03	0.04	0.05	0.09	0.09	0.16	0.23	0.30	0.64	0.58	1.98	1.82	6.54	0	8.77	2.94
19	0.01	0.01	0.01	0.01	0.01	0.02	0.02	0.04	0.04	0.07	0.08	0.14	0.19	0.27	0.56	0.55	1.83	1.70	6.54	0	8.94
20	0	0	0	0.01	0.01	0.01	0.01	0.02	0.03	0.03	0.06	0.06	0.12	0.16	0.25	0.48	0.52	1.67	1.60	6.52	0

rate constants with increasing $|\Delta E|$ that was needed to account for the kinetic data resulted in artificially low pressure broadening coefficients for the higher J levels. In contrast, the rate constants and pressure broadening coefficients derived from the SAPT potential were more consistent with energy transfer controlled by the momentum gaps.^{43,44} This inference is in agreement with the findings of BelBruno *et al.*,³⁵ who noted that the impulsive CO rotational energy transfer involving He was qualitatively different from RET induced by CO+CO collisions. The latter, typical of transfer induced by a heavy collision partner, appears to be energy gap dependent.^{30,35}

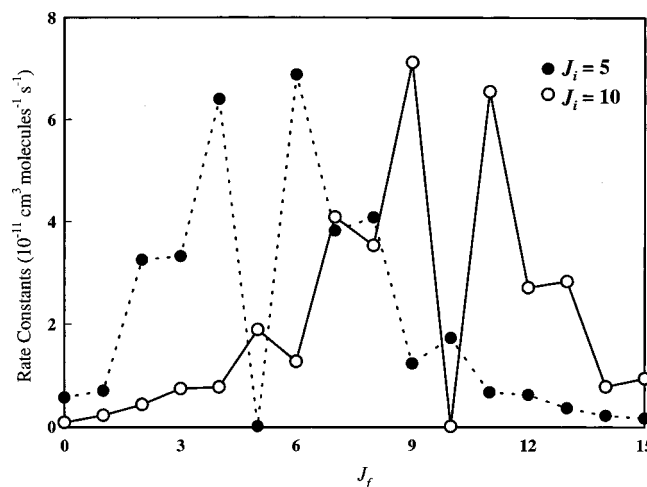


FIG. 11. Rate constants derived from the SAPT potential energy surface. The solid points and open circles correspond to $J_i=5$ and 10, respectively. The maximum in the Boltzmann distribution occurs at $J=7$. Hence the rate constants for $J_i=5$ favor upward transfer while those for $J_i=10$ favor downward transfer. Note that the rate constants show a clear preference for odd ΔJ transitions.

ACKNOWLEDGMENTS

We are grateful to the Air Force Office of Scientific Research (AFOSR) for support of this research. Authors T.C.S. and D.A.H. would like to thank the National Research Council for postdoctoral fellowships. M.C.H. thanks AFOSR for support through Grant No. AFOSR F49620-02-1-0357.

- M. Thachuk, C. E. Chuaqui, and R. J. Le Roy, *J. Chem. Phys.* **105**, 4005 (1996).
- E. L. Heck and A. S. Dickinson, *Mol. Phys.* **91**, 31 (1997).
- S. Antonova, A. Lin, A. P. Tsakotellis, and G. C. McBane, *J. Chem. Phys.* **110**, 2384 (1999).
- F. A. Gianturco, F. Paesani, M. F. Laranjeira, V. Vassilenko, M. A. Cunha, A. G. Shashkov, and A. F. Zolotoukhina, *Mol. Phys.* **92**, 957 (1997).
- P. Duggan, P. M. Sinclair, R. Berman, A. D. May, and J. R. Drummond, *J. Mol. Spectrosc.* **186**, 90 (1997).
- P. Duggan, P. M. Sinclair, A. D. May, and J. R. Drummond, *Phys. Rev. A* **51**, 218 (1995).
- M. M. Beaky, T. M. Goyette, and F. C. De Lucia, *J. Chem. Phys.* **105**, 3994 (1996).
- H. P. Butz, R. Feltgen, H. Pauly, and H. Vehmeyer, *Z. Phys.* **247**, 70 (1971).
- M. Keil, J. T. Slankas, and A. Kuppermann, *J. Chem. Phys.* **70**, 541 (1979).
- M. Faubel, K. H. Kohl, and J. P. Toennies, *J. Chem. Phys.* **73**, 2506 (1980).
- E. J. Kruus, *J. Phys. Chem.* **98**, 3099 (1994).
- D. Bassi, A. Boschetti, S. Marchetti, G. Scoles, and M. Zen, *J. Chem. Phys.* **74**, 2221 (1981).
- M. M. Ahern, D. A. Steinhurst, and M. A. Smith, *Chem. Phys. Lett.* **300**, 681 (1999).
- L. D. Thomas, W. P. Kraemer, and G. H. F. Dierksen, *Chem. Phys.* **51**, 131 (1980).
- C. E. Chuaqui, R. J. Le Roy, and A. R. W. McKellar, *J. Chem. Phys.* **101**, 39 (1994).
- M.-C. Chan and A. R. W. McKellar, *J. Chem. Phys.* **105**, 7910 (1996).
- A. R. W. McKellar, Y. Xu, W. Jäger, and C. Bissonnette, *J. Chem. Phys.* **110**, 10766 (1999).
- L. A. Surin, D. A. Roth, I. Pak, B. S. Dumes, F. Lewen, and G. Winnewisser, *J. Chem. Phys.* **112**, 4064 (2000).

- ¹⁹L. A. Surin, D. A. Roth, I. Pak, B. S. Dumes, F. Lewen, and G. Winnewisser, *J. Chem. Phys.* **112**, 9190 (2000).
- ²⁰F. A. Gianturco and F. Paesani, *Mol. Phys.* **99**, 689 (2001).
- ²¹R. Kobayashi, R. D. Amos, J. P. Reid, H. M. Quiney, and C. J. S. M. Simpson, *Mol. Phys.* **98**, 1995 (2000).
- ²²T. G. A. Heijmen, R. Moszynski, P. E. S. Wormer, and A. van der Avoird, *J. Chem. Phys.* **107**, 9921 (1997).
- ²³R. Moszynski, T. Korona, P. E. S. Wormer, and A. van der Avoird, *J. Chem. Phys.* **103**, 321 (1995).
- ²⁴F. A. Gianturco, N. Sanna, and S. Serna-Molinera, *Mol. Phys.* **81**, 421 (1994).
- ²⁵R. J. Le Roy, C. Bissonnette, T. H. Wu, A. K. Dham, and W. J. Meath, *Faraday Discuss.* **97**, 81 (1994).
- ²⁶F.-M. Tao, S. Drucker, R. C. Cohen, and W. Klemperer, *J. Chem. Phys.* **101**, 8680 (1994).
- ²⁷B. Kukawska-Tarnawska, G. Chalasiński, and K. Olszewski, *J. Chem. Phys.* **101**, 4964 (1994).
- ²⁸J. J. Klaassen, S. L. Coy, J. I. Steinfeld, and B. Abel, *J. Chem. Phys.* **101**, 10533 (1994); J. J. Klaassen, S. L. Coy, J. I. Steinfeld, and Ch. Roche, *ibid.* **100**, 5519 (1994); C. C. Flannery, J. I. Steinfeld, and R. R. Gamache, *ibid.* **99**, 6495 (1993).
- ²⁹K. P. Huber and G. Herzberg, *Molecular Spectra and Molecular Structure-IV: Constants of Diatomic Molecules* (Van Nostrand-Reinhold, New York, 1979).
- ³⁰S. P. Phipps, T. C. Smith, G. D. Hager, M. C. Heaven, J. K. McIver, and W. G. Rudolph, *J. Chem. Phys.* **116**, 9281 (2002).
- ³¹J. E. McCord, H. C. Miller, G. D. Hager, A. I. Lampson, and P. G. Crowell, *IEEE J. Quantum Electron.* **35**, 1602 (1999).
- ³²J. E. McCord, A. A. Ionin, S. P. Phipps, P. G. Crowell, A. I. Lampson, J. K. McIver, A. J. W. Brown, and G. D. Hager, *IEEE J. Quantum Electron.* **36**, 1041 (2000).
- ³³G. D. Billing, in *Nonequilibrium Vibrational Kinetics*, edited by M. Capitelli (Springer Verlag, Berlin, 1986).
- ³⁴J. I. Steinfeld, P. Ruttenger, G. Millot, G. Fanjoux, and B. Lavorel, *J. Phys. Chem.* **95**, 9638 (1991) and references therein.
- ³⁵J. J. BelBruno, J. Gelfand, and H. Rabitz, *J. Chem. Phys.* **78**, 3990 (1983).
- ³⁶R. J. Le Roy, *LEVEL 7.4: A Computer Program for Solving the Radial Schrödinger Equation for Bound and Quasibound Levels*, University of Waterloo, Chemical Physics Report CP-642 R3 (2001). The source code and manual for this computer program can be obtained on the WWW site <http://leroy.uwaterloo.ca>.
- ³⁷J. M. Hutson and S. Green, MOLSCAT computer code, version 14 (1994), distributed by Collaborative Computational Project No. 6 of the Engineering and Physical Sciences Research Council (UK).
- ³⁸M. H. Alexander and D. E. Manolopoulos, *J. Chem. Phys.* **86**, 2044 (1987).
- ³⁹A. G. Maki, J. S. Wells, and D. A. Jennings, *J. Mol. Spectrosc.* **144**, 224 (1990).
- ⁴⁰P. McGuire and D. J. Kouri, *J. Chem. Phys.* **60**, 2488 (1974).
- ⁴¹J. I. Steinfeld and R. R. Gamache, *Spectrochim. Acta, Part A* **54**, 65 (1998).
- ⁴²J. J. BelBruno, J. Gelfand, W. Radigan, and K. Verges, *J. Mol. Spectrosc.* **94**, 336 (1982).
- ⁴³A. J. McCaffery, Z. T. Alwahabi, M. A. Osborne, and C. J. Williams, *J. Chem. Phys.* **98**, 4586 (1993).
- ⁴⁴M. Osborne and A. J. McCaffery, *J. Chem. Phys.* **101**, 5604 (1994).